








A New Extraction Method of Surface Water Based on Dense Time-Sequence Images

Hanyuan Liu , Yue Shi, Qinnan Chang, Rufat Guluzade , Xin Pan , Nan Xu , Penghua Hu ,
Xuechun Kong , and Yingbao Yang 

Abstract—Fluctuations in the surface water are indicators of climatic and biological environmental variations. The water index method is the predominant approach for water extraction owing to its simplicity of operation and high efficiency. Recognizing the limitations of individual water indices in extracting water over dense time-sequences, this study introduces a combined water index (CWI) frequency method to improve the water extraction results. The research findings indicate the following: 1) CWI demonstrates superior extraction accuracy for various types of water when compared with other water indices, underscoring its higher precision and broader applicability. 2) By integrating CWI with the water frequency method, we propose an effective approach for dynamically monitoring water. This method accurately reflects changes in water under different conditions within dense time-sequence images. 3) Our results highlight the method's ability to precisely monitor dynamic water changes, efficiently extract various water types from Sentinel-2 data, and its potential for large-scale surface water mapping applications.

Index Terms—Combined water index (CWI), dense time-sequence images, dynamic changes of water, surface water, water frequency.

I. INTRODUCTION

SURFACE water has immense significance for both the sustenance and development of all living beings. In addition, it plays a pivotal role in regional ecological environment assessment [1], [2], [3], [4], judicious planning of water resources, and facilitating human life and social activities [5], [6], [7], [8], [9]. Traditional water monitoring methods are labor-intensive, time-consuming, and often lack real-time capabilities. Remote sensing technology, with its attributes of large-scale coverage,

Manuscript received 30 October 2023; revised 1 December 2023; accepted 27 December 2023. Date of publication 1 January 2024; date of current version 18 January 2024. This work was supported in part by the General Programs of the National Natural Science Foundation of China under Grant 42371397 and Grant 42071346, in part by the Jiangsu Marine Science and Technology Innovation Project JSZRHYKJ202302, and in part by the National Natural Science Foundation of China (NSFC) under Grant 42101343. (*Hanyuan Liu and Yue Shi contributed equally to this work.*) (Corresponding author: Yingbao Yang.)

Hanyuan Liu, Rufat Guluzade, Penghua Hu, and Xuechun Kong are with the School of Earth Sciences and Engineering, Hohai University, Nanjing 211100, China (e-mail: hhulihanyuan@163.com; rufat.guluzade@hhu.edu.cn; hupenghua2020@163.com; kxc415@163.com).

Yue Shi is with the College of Defense Engineering, The Army Engineering University of PLA, Nanjing 210007, China (e-mail: yues_1984@163.com).

Qinnan Chang is with the Jincheng Urban District Housing and Urban-Rural Development Bureau, Shanxi 048000, China (e-mail: qnchang@hhu.edu.cn).

Xin Pan, Nan Xu, and Yingbao Yang are with the College of Geography and Remote Sensing, Hohai University, Nanjing 211100, China (e-mail: px1013@hhu.edu.cn; hhuxunan@gmail.com; yyb@hhu.edu.cn).

Digital Object Identifier 10.1109/JSTARS.2023.3348488

high precision, and real-time imaging, is widely applied in water extraction [10], [11], [12], [13].

The prevailing approaches for extracting water from remote sensing images include classification and water index methods. Methods based on classifiers were employed to extract features derived from the physical and geographical attributes of the images. Water and nonwater regions were differentiated based on the criteria of minimal internal variance and maximal interclass variance. These variables were subsequently utilized to classify areas as either water or nonwater based on their proximity to the statistical center. Decision-tree models [14], support vector machine (SVM) models [15], and object-oriented methods [16] have been widely used for classification. The core principle of the decision tree classification method is to consolidate the essential conditions for refining the initial data, thereby enabling precise pixel classification through the decision tree [17]. This approach exhibits the notable flexibility and operates with high efficiency. SVMs are capable of achieving improved classification results with fewer samples [18]. However, they exhibit limitations in terms of accurately delineating river boundaries and identifying small water. The object-oriented method employs various algorithms to efficiently extract the target image information from objects containing pixels of varying sizes and homogeneity [16]. This approach mitigates the impact of factors such as ground object shadows and enables the high-precision extraction of small water pixels. Nevertheless, classification methods require substantial prior knowledge, leading to complex models that are sensitive to the influence of intricate background environments on the classification outcomes.

Water feature information can be derived from a vast dataset using deep learning, and water extraction is achieved by constructing a suitable network structure. Currently, various deep learning algorithms have been applied to research on water extraction [19], [20]. A two-stage method based on deep learning, capable of extracting narrower or smaller rivers, was proposed by Fei et al. [21]. Wang et al. [22] presented a water extraction method that combines deep learning with Google Earth Engine (GEE) platforms, designed for investigating large-scale, long-term urban moisture changes amid urbanization. Isikdogan et al. [23] introduced a fully neural network utilizing only Landsat bands, eliminating the need for additional auxiliary data. However, it is noteworthy that the continuity of water is often compromised during deep learning extraction, leading to delayed results and the inability to promptly rectify inaccuracies.

The water index method is an approach for collecting water information based on the original single-band threshold method and the combined operation of the bands [24]. The principle of the water index method is to use water information to construct operations in bands with strong and weak reflection characteristics in the spectrum. The characteristic difference between the bands was further intensified to improve water information and suppress nonwater information [25]. The water index method has the advantages of a simple format and easy application; therefore, it is widely used in research on optical image extraction of water. Scholars have designed various water indices based on the multispectral bands. The normalized difference water index (NDWI) was proposed by McFEETERS in 1996, which was a significant breakthrough in water resource extraction [26]. However, when using NDWI for water extraction, water pixels are usually mixed with the land noise of the built-up area, resulting in an overestimation of the water area. Therefore, Xu [27] constructed a modified NDWI (MNDWI) that can enhance the water information of water areas with built-up areas as the background. Although MNDWI enhances the difference between water pixels and built-up background pixels, it cannot separate water from mountains and hill shades [24]. To eliminate the influence of hill shadows, Ronglong et al. [28] used short-wave infrared and red bands of TM images to create a revised NDWI (RNDWI) for water extraction. RNDWI weakens the influence of mixed pixel factors and hill shadows and can accurately extract land and water boundaries.

The above-mentioned water indices only consider information from two bands, resulting in relatively low applicability of the water indices. Feyisa et al. [29] designed an automated water extraction index (AWEI) that was divided into two parts: $AWEI_{sh}$ and $AWEI_{nsh}$. By applying different coefficients to the five spectral bands for addition and subtraction, AWEI has higher accuracy and a more stable threshold for water extraction under various environmental noises. Li et al. [30] fully considered the local spatial information of the image, weighted the water indices according to the spatial information, and constructed the background difference water index, which improved the stability of water extraction under different backgrounds.

The spatiotemporal changes in surface water resources have a profound impact on ecosystem preservation and sustainable economic development and are closely linked to water scarcity concerns. The current investigation into long-term surface water dynamics not only examines the instantaneous state of water but also underscores the need for an in-depth comprehension of the spatiotemporal evolution rules governing changes in water. The primary focus of this research lies in the utilization of optical and synthetic aperture radar image data to formulate continuous extraction methodologies for long-term surface water assessment. This involves an analysis of seasonal, interannual, and long-term trend variations in water, revealing dynamic characteristics over distinct periods. In addition, the examination extends to alterations in water area and the mechanisms influenced by diverse factors, such as climate and human activities. Scholars have extensively employed multisource data fusion and multiscale analysis techniques to comprehensively integrate remote sensing data, ground observations, hydrological model simulations, and

other multisource data. This holistic approach serves to enhance the precision of water monitoring and global research coverage, thereby offering multifaceted support for water resource management across various scales [31], [32], [33].

Large-scale surface water has complex backgrounds and various types of shorelines [34]. The use of a single water index has significant limitations as it cannot accurately extract water. In this study, we present a combined water index (CWI) model designed for the accurate extraction of water across diverse environmental conditions. The CWI model enhances the universality and accuracy of water extraction methods. In addition, we employed the CWI model in conjunction with water frequency methods to develop a technique for calculating the average water area within dense time-sequence datasets. The computation of the average water area holds significant importance for water environment and resources management. By monitoring the average area of water, valuable insights into the health of the water ecosystem and the equilibrium between water supply and demand can be gained. This, in turn, facilitates the formulation of more effective water resources management strategies, contributing to the protection of water resources and biodiversity, and ensuring the sustainable utilization of water resources.

II. STUDY AREA AND DATA

A. Study Area

Jiangsu Province is located in the eastern coastal area of mainland China, with a longitude of $116^{\circ}21' - 121^{\circ}56'E$ and a latitude of $30^{\circ}45' - 35^{\circ}08'N$ (Fig. 1). There are 1495 rivers in Jiangsu, with a drainage area of 50 km^2 or more, and a total length of more than 40 000 km. It is worth mentioning that two of China's five largest freshwater lakes are located there, with Lake Taihu covering 2250 km^2 and Lake Hongze covering 2069 km^2 . Jiangsu Province has a total of 908 reservoirs, including 6 large, 42 medium, and 860 small reservoirs.

Jiangsu Province is endowed with ample water resources and diverse water types. In this study, water in urban area (area A), vegetation area (area B), and mountainous area (area C) are chosen (Fig. 2) to test the usefulness of the CWI for water extraction in large-scale, complex, and changing environments.

B. Dataset

Sentinel-2 is an advanced high-resolution multispectral imaging satellite equipped with a multispectral imager featuring 13 spectral bands. These bands span across visible light, near-infrared, and short-wave infrared regions, each offering different spatial resolutions [35]. Sentinel-2 is frequently employed for capturing imagery pertinent to parameters such as vegetation, soil composition, water coverage, inland waterways, and coastal regions. Therefore, Sentinel-2 is extensively employed in water extraction research.

Based on the changing characteristics of water in different seasons in Jiangsu Province, images with the smallest cloud cover in February, May, July, and November were selected as the experimental data (Table I).

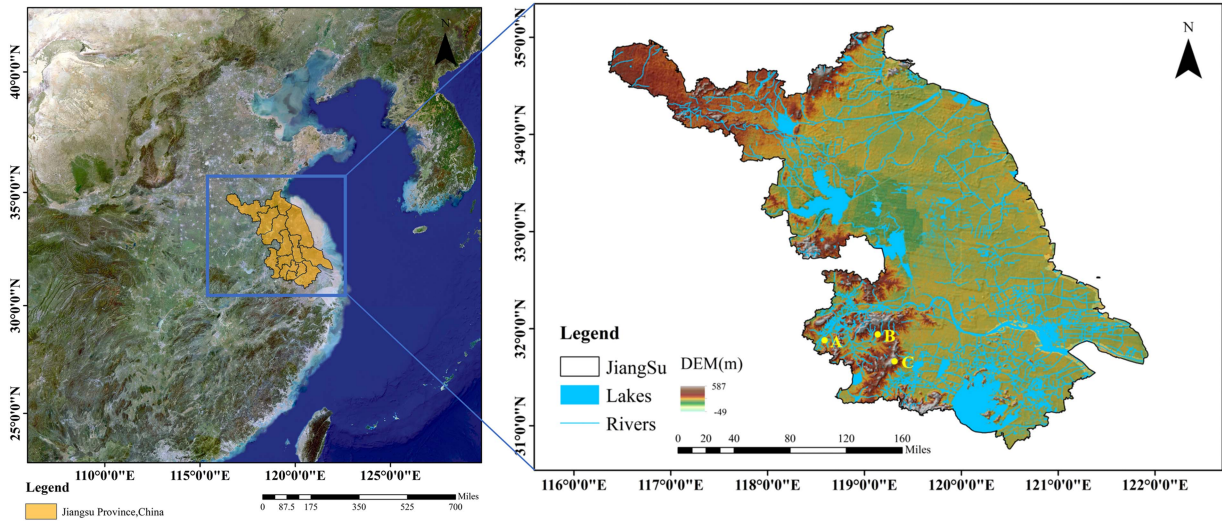


Fig. 1. Basic information of Jiangsu Province.

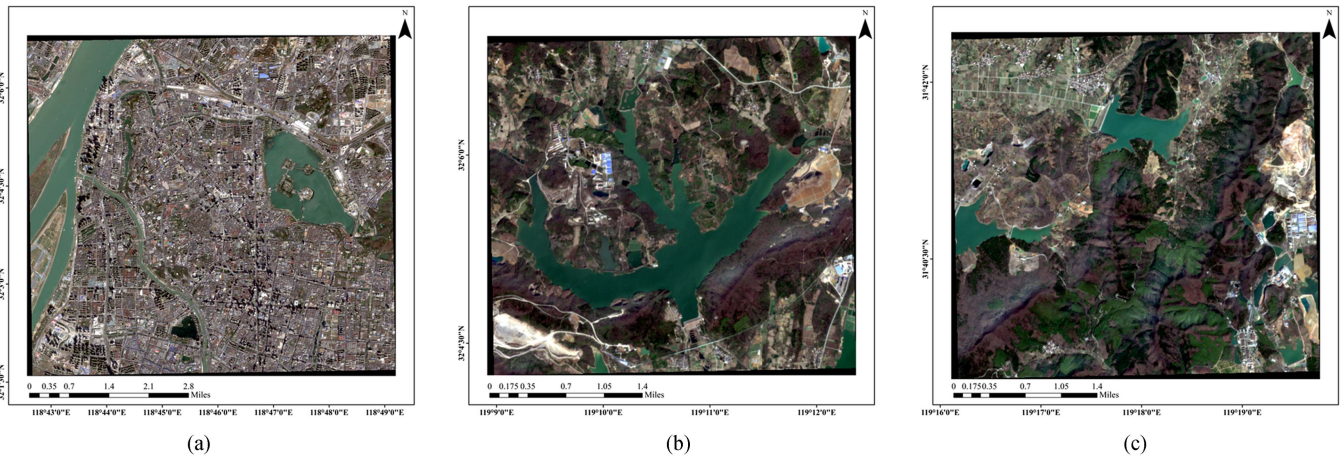


Fig. 2. Basic information of the experiment area. (a) Urban area. (b) Vegetation area. (c) Mountainous area.

TABLE I
EXPERIMENTAL DATA INFORMATION

Research area	Month	Cloud cover (%)
Urban area	February	0.51
	May	0.87
	July	1.2
	November	0.43
Vegetation area	February	0.51
	May	0.88
	July	1.19
	November	0.43
Mountainous area	February	0.72
	May	3.0
	July	3.9
	November	0.65

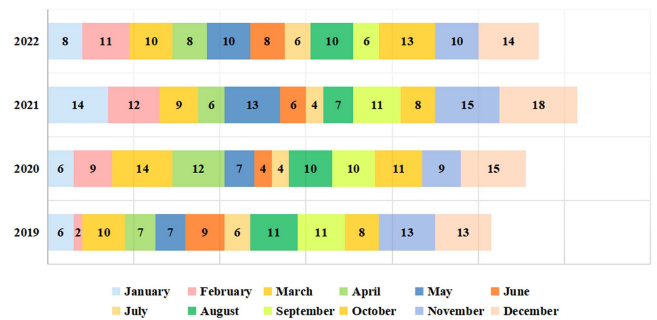


Fig. 3. Annual image quantity.

To realize water extraction from intensive time-sequence images, the experiment selected image data with an annual cloud cover of less than 10% from 2019 to 2022. The annual image coverage is shown in Fig. 3. The source of the Sentinel-2 image

in this study is the Sentinel-2 L2A product on the GEE platform. The Sentinel-2 L2A product undergoes atmospheric correction, utilizing the Sen2Cor processor for this purpose. Specifically designed for the Sentinel-2 environment, the Sen2Cor processor addresses atmospheric effects present in the Sentinel-2 1C

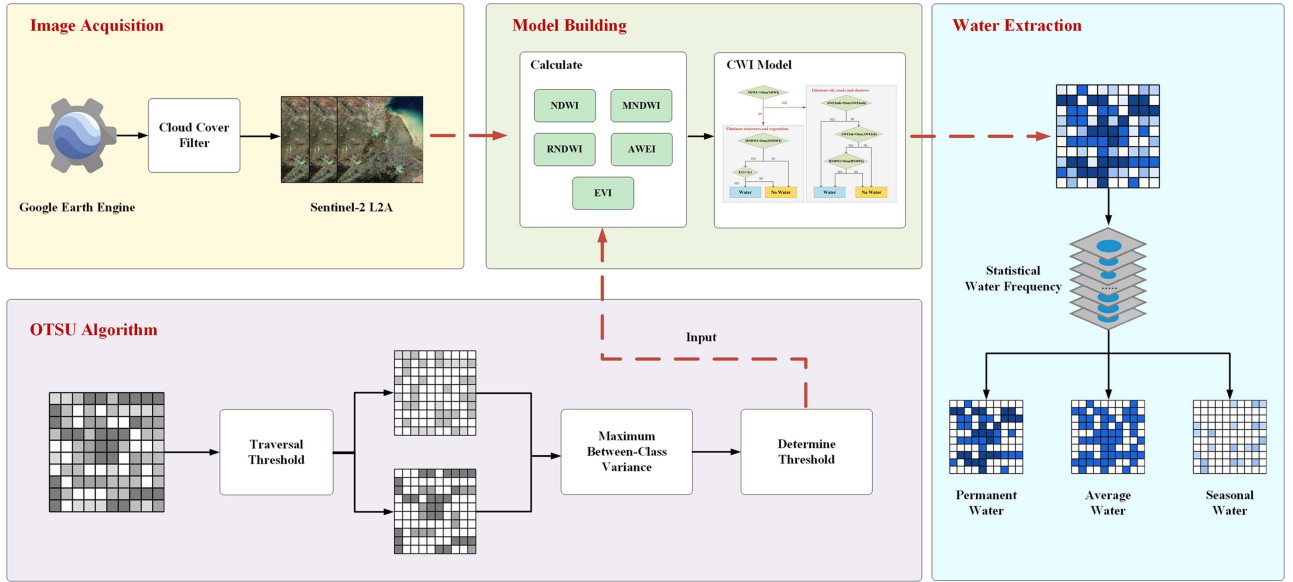


Fig. 4. Flow chart to extract water.

TABLE II
WATER INDEX RELATED INFORMATION (ρ STANDS FOR REFLECTIVITY, SUBSCRIPT IS THE NAME OF THE BAND)

Index	Formula	Features
NDWI [26]	$NDWI = \frac{\rho_{Green} - \rho_{NIR}}{\rho_{Green} + \rho_{NIR}}$	Eliminating soil and terrestrial vegetation features
MNDWI [27]	$MNDWI = \frac{\rho_{Green} - \rho_{SWIR1}}{\rho_{Green} + \rho_{SWIR1}}$	Enhance open water features and suppress built-up land noise
RNDWI [28]	$RNDWI = \frac{\rho_{SWIR1} - \rho_{Red}}{\rho_{SWIR1} + \rho_{Red}}$	Reduce the effect of mixed pixel factors and hillshade
AWEI [29]	$AWEI_{sh} = \rho_{Blue} + 2.5 \times \rho_{Green} - 1.5 \times (\rho_{NIR} + \rho_{SWIR1}) - 0.25 \times \rho_{SWIR2}$ $AWEI_{nsh} = 4 \times (\rho_{Green} - \rho_{SWIR1}) - (0.25 \times \rho_{NIR} + 2.75 \times \rho_{SWIR2})$	Maximize separability of water and nonwater pixels
EVI [37]	$EVI = 4 \times \frac{\rho_{NIR} - \rho_{Red}}{\rho_{NIR} + 6 \times \rho_{Red} - 7 \times \rho_{Blue} + 1}$	Increased vegetation sensitivity

top-of-atmosphere product, ultimately generating a Class 2A bottom-of-atmosphere reflectance product [36].

III. METHODOLOGY

The process of this research is shown in Fig. 4, which comprises four primary components: image preprocessing, model construction, threshold selection, and water extraction. The following sections provide detailed explanations of the latter three components.

A. Building the Water Extraction Framework

Various water indices have specific applications. Therefore, researchers using only one water index cannot remove background interference from various ground objects. Table II lists the calculation formulas and applicable ranges for the various types of water indices. The CWI framework is developed based on the main ground object interference factors and applicability of various water indices in the process of water extraction. The

primary objective is to broaden the scope of application of water extraction methods, enabling the accurate water extraction even in complex environments.

Fig. 5 shows the calculation method of CWI. According to the applicable range outlined in Table II for various water indices, the CWI is divided into three distinct parts. The first segment employs NDWI to identify the majority of water pixels. In the second part, the focus is on mitigating the influence of buildings and vegetation. Despite NDWI's effectiveness in identifying water, there is a tendency for a few water pixels to be misclassified as dark buildings and subsequently overlooked. To address this, MNDWI is introduced to alleviate building interference. In addition, when the enhanced vegetation index value of a pixel is below 0.1, it signifies an opportunity to eliminate vegetation interference [37]. This step allows for the complete extraction of water in densely built areas. In the third part, efforts are made to eliminate the effects of mud, roads, and shadows. The $AWEI_{nsh}$ index, in combination with the RNDWI index, facilitates the distinction between silt and water.

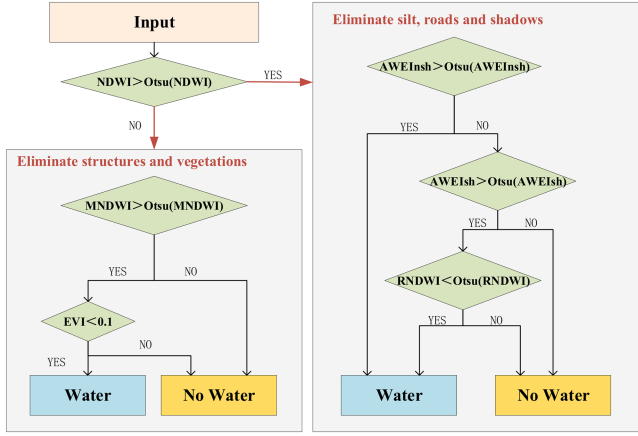


Fig. 5. Water extraction framework based on water and vegetation indices. (Otsu is the threshold determination method in this article, which is explained in detail in Section III-B).

Notably, areas with mixed pixels in the water, as extracted using NDWI, can benefit from $AWEI_{nsh}$ to eliminate interference from dark buildings and roads, particularly in regions less affected by shadows. $AWEI_{sh}$, on the other hand, proves effective in eliminating shadow interference in areas where shadows pose a more significant challenge. Building upon these steps, RNDWI is employed to screen and extract the land-water interface area, culminating in the final and comprehensive delineation of water.

B. Determining the Threshold

Threshold selection methods enhance the practicality of water indices compared to using a fixed threshold value. Otsu thresholding is a highly efficient and widely adopted threshold determination method, particularly for water extraction.

The fundamental principle of Otsu thresholding is to explore all possible thresholds and analyze and count the two types of pixels resulting from the threshold segmentation. Through statistical analysis, the threshold value between two types of pixels can be identified swiftly [38], [39]. The principle of the algorithm is as follows.

In image $I(x, y)$, the thresholds are divided based on gray levels $1, 2, 3, \dots, M$. The probability of each gray level i is

$$P_i = \frac{n_i}{N} \quad (1)$$

where N represents the total number of pixels, and P_i represents the number of pixels with gray level i .

Assume that the image contains foreground pixels with a proportion of ω_0 and background pixels with a proportion of ω_1 . In addition, the average gray levels for the foreground and background are represented as μ_0 and μ_1 , respectively. The formula used is as follows:

$$\omega_0 = \sum_{i=1}^T P_i \quad (2)$$

$$\omega_1 = \sum_{i=T+1}^M P_i \quad (3)$$

$$\mu_0 = \sum_{i=1}^T \frac{iP_i}{\omega_0} \quad (4)$$

$$\mu_1 = \sum_{i=T+1}^M \frac{iP_i}{\omega_1} \quad (5)$$

The average gray level is

$$\mu = \omega_0 \times \mu_0 + \omega_1 \times \mu_1. \quad (6)$$

The interclass variance (g) of the foreground and background pixels is

$$g = \omega_0 \times (\mu - \mu_0)^2 + \omega_1 \times (\mu - \mu_1)^2. \quad (7)$$

Therefore, the optimal threshold (T) is

$$T = \operatorname{argmax}(g). \quad (8)$$

C. Calculating Average Water Area

Water exhibits dynamic characteristics, and the synthetic results obtained from only one image or a composite image fail to adequately capture the dynamic changes in water. Therefore, the water frequency method is incorporated into this experiment to capture the dynamic change characteristics.

The CWI frequency method is divided into two parts: water pixel identification and water frequency calculation. Formula (9) is used to identify water pixels based on the CWI framework, representing nonwater and water with 0 and 1 values, respectively. Formula (10) is employed to calculate the frequency of each pixel in the dense time-series image identified as a water pixel. $\sum N_{Water}$ is the number of pixels identified as water, and $\sum N_{Total}$ is the total number of observations.

$$CWI = \begin{cases} 1, & \text{Water} \\ 0, & \text{Non-Water} \end{cases} \quad (9)$$

$$F_{Water} = \frac{\sum N_{Water}}{\sum N_{Total}} \quad (10)$$

F_{Water} represents the water frequency at each pixel location. Water is categorized into four types based on the water frequency: permanent water ($F_{Water} \geq 0.75$), seasonal water ($0.25 \leq F_{Water} < 0.75$), temporary water ($F_{Water} < 0.25$) [40], [41], [42], and average water. In formula (11), the average surface water area ($S_{average}$) is calculated as the sum of the water frequency multiplied by the pixel area of all effective water corresponding to it ($S_{F_{Water}}$).

$$S_{average} = \sum F_{Water} * S_{F_{Water}}. \quad (11)$$

D. Evaluating Accuracy of Water Extraction

In the experiments, we utilized the confusion matrix to compute both the overall classification accuracy and the Kappa coefficient [43]. The overall classification accuracy is the ratio of the total number of correctly classified samples to the total number of samples in the experimental area, and reflects the accuracy of the overall extraction results. The Kappa coefficient can measure classification accuracy and examine consistency [44].

TABLE III
OA AND KAPPA IN URBAN AREA

Month		CWI	NDWI	MNDWI	RNDWI	AWEI _{sh}	AWEI _{nsh}
February	OA(%)	96.85	96.43	96.43	96.22	84.66	87.61
	Kappa	0.93	0.92	0.92	0.92	0.65	0.72
May	OA(%)	95.17	93.14	94.63	89.15	76.58	93.88
	Kappa	0.90	0.86	0.89	0.78	0.51	0.88
July	OA(%)	95.09	91.20	94.78	90.48	82.91	94.68
	Kappa	0.90	0.82	0.90	0.81	0.65	0.89
November	OA(%)	95.98	95.69	95.49	93.93	76.00	90.89
	Kappa	0.92	0.91	0.91	0.88	0.51	0.82
Average	OA(%)	95.77	94.12	95.33	92.45	80.04	91.77
	Kappa	0.91	0.88	0.91	0.85	0.58	0.83

The highest value of all OA/Kappa.

The accuracy assessment in this study mainly includes three steps: 1) In each experimental area, randomly generate a set of 500 water sample points and another set of 500 nonwater sample points; 2) Utilize Google Earth as a reference for the examination and correction of randomly generated sample points; 3) Quantitatively evaluate the water extraction accuracy using both the overall classification accuracy and the Kappa coefficient.

IV. RESULTS

In this study, the CWI method was applied to extract water from urban area, vegetation area, and mountainous area during various seasons. In addition, the water frequency in Jiangsu Province was computed from 2019 to 2022. The subsequent sections provide an analysis of water extraction results.

A. Water Extraction Results in Urban Area

Dark buildings and shadows are frequently mistaken for water in urban areas. Lake Xuanwu, located in the center of Nanjing with a high degree of urbanization and close proximity between buildings and water, is selected as the experimental area for this study. The extraction results are shown in Fig. 6. During the same season, there is a lot of shadow noise, and numerous structures, such as roads and buildings, are misclassified as water by AWEI_{sh} and AWEI_{nsh}. Other water indices can effectively extract the majority of the water, albeit with detailed variations. In the densely populated metropolitan region located to the south of the experimental area, the NDWI extraction results for July and November exhibit some noise (as shown in red circles). During May and July, RNDWI exhibited incorrect identification of Lake Mochou, which is situated to the south of the experimental area (as shown in green circles). In contrast, because MNDWI increases the distinction between water and buildings, the impact of buildings on the extraction outcomes is marginal. Given that CWI incorporates the benefits of several water indices, it can consistently achieve favorable extraction results across various seasons and under varying water conditions.

Table III shows that the average overall accuracy (OA) for CWI was 95.77%, with an average kappa coefficient of 0.91. These averages are 0.44% and 0.01 higher, respectively, than those of the MNDWI in terms of accuracy. The experimental results indicate that CWI can suppress structures and shadows more effectively than alternative water indices and that the results of the extraction are almost completely consistent with

real water. Thus, CWI has emerged as an optimal method for computing dense time-sequences water areas in urban settings.

B. Water Extraction Results in Vegetation Area

The experiment also focused on the selection of water within vegetated areas to assess the anti-interference capabilities of various approaches. The experimental area was located in the west of Jiangsu Province, with dense vegetation and complex water boundaries. The water extraction results for various water indices in the vegetation area are shown in Fig. 7.

During the same season, vegetation can be effectively distinguished from water using a variety of water indices, resulting in a clearly defined boundary between them. In May and July, clear misclassifications were observed for NDWI and RNDWI in the eastern barren area, and AWEI_{sh} also exhibited misclassifications in July at this location (as shown in red circles). In July, water extraction by AWEI_{nsh} in the central part of the experimental area was inefficient, and the quality of the water classification was suboptimal (as shown in green circle). In this area, the MNDWI yields comprehensive water extraction results with minimal noise; however, its capacity to detect small water is limited. In addition to its superior vegetation control capabilities, CWI exhibited a greater capacity for detecting small water within the southern portion of the experimental region and outperformed other techniques in water extraction (as shown in black circles).

The water extraction accuracy in vegetation area is shown in Table IV. Within the vegetated region, CWI achieved the highest average OA and an average kappa coefficient of 96.74% and 0.93, respectively, surpassing the second-ranked AWEI_{nsh} by 1.07% and 0.02, respectively. Across various seasons, CWI consistently exhibits higher OA and Kappa coefficients than alternative approaches, substantiating its superiority as the preferred method for estimating water areas within vegetated regions.

C. Water Extraction Results in Mountainous Area

The terrain in mountainous areas is characterized by its complexity and numerous shaded areas. The waters of the southern hilly region of Jiangsu Province were selected to evaluate the extraction effectiveness of the diverse water indices. Fig. 8 shows the water extraction results obtained using various methods in mountainous area.

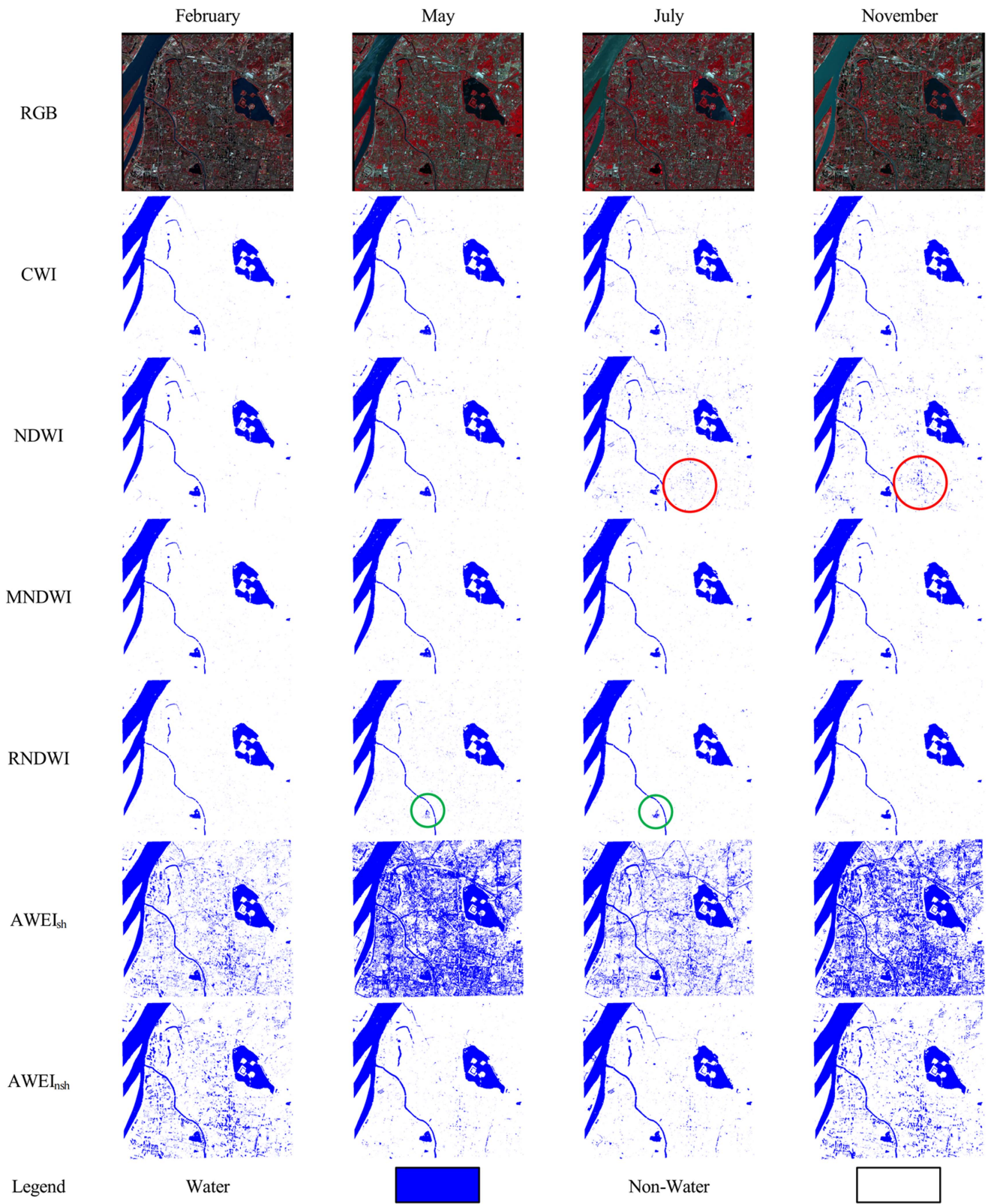


Fig. 6. Water extraction results in urban area.

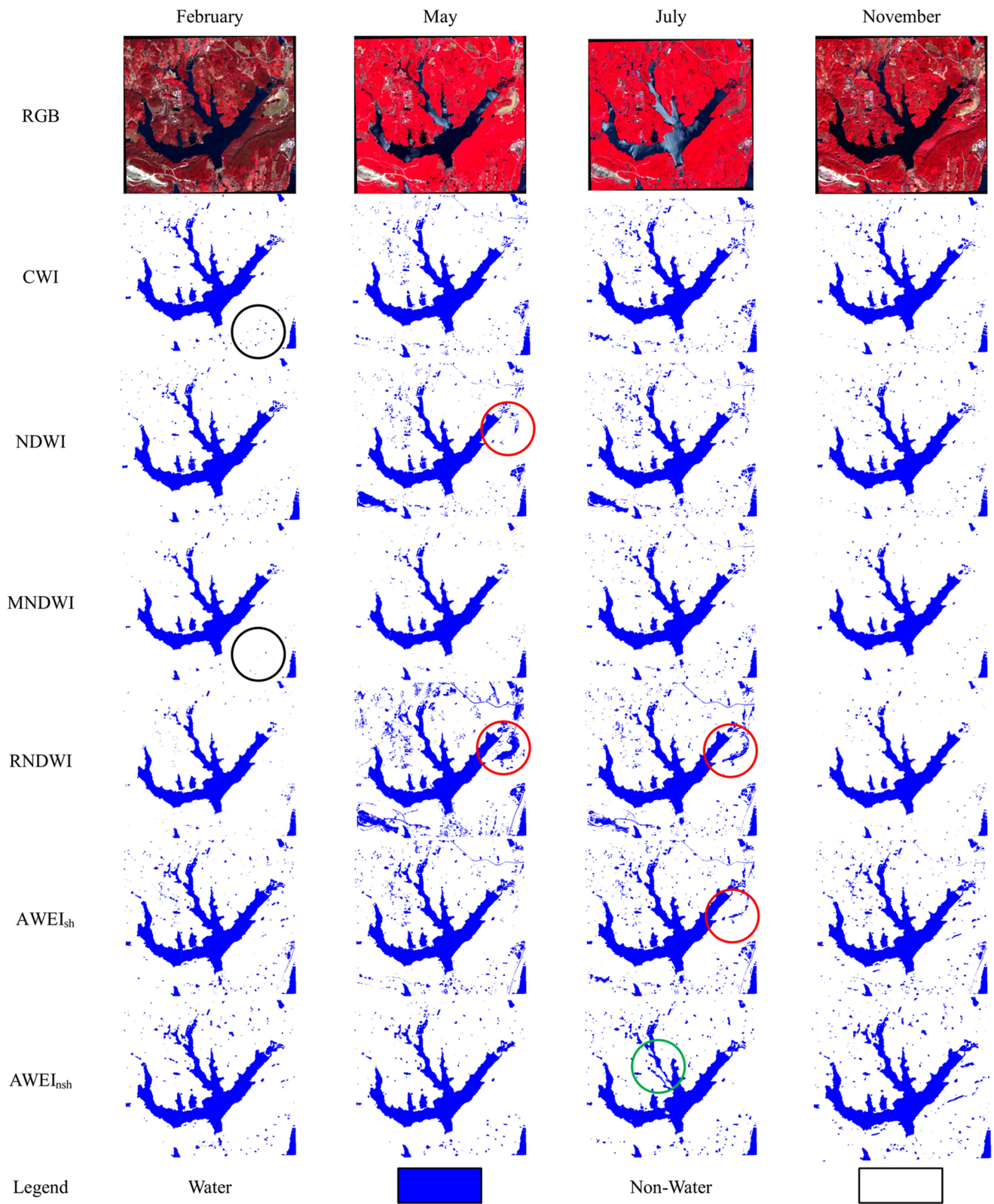


Fig. 7. Water extraction results in vegetation area.

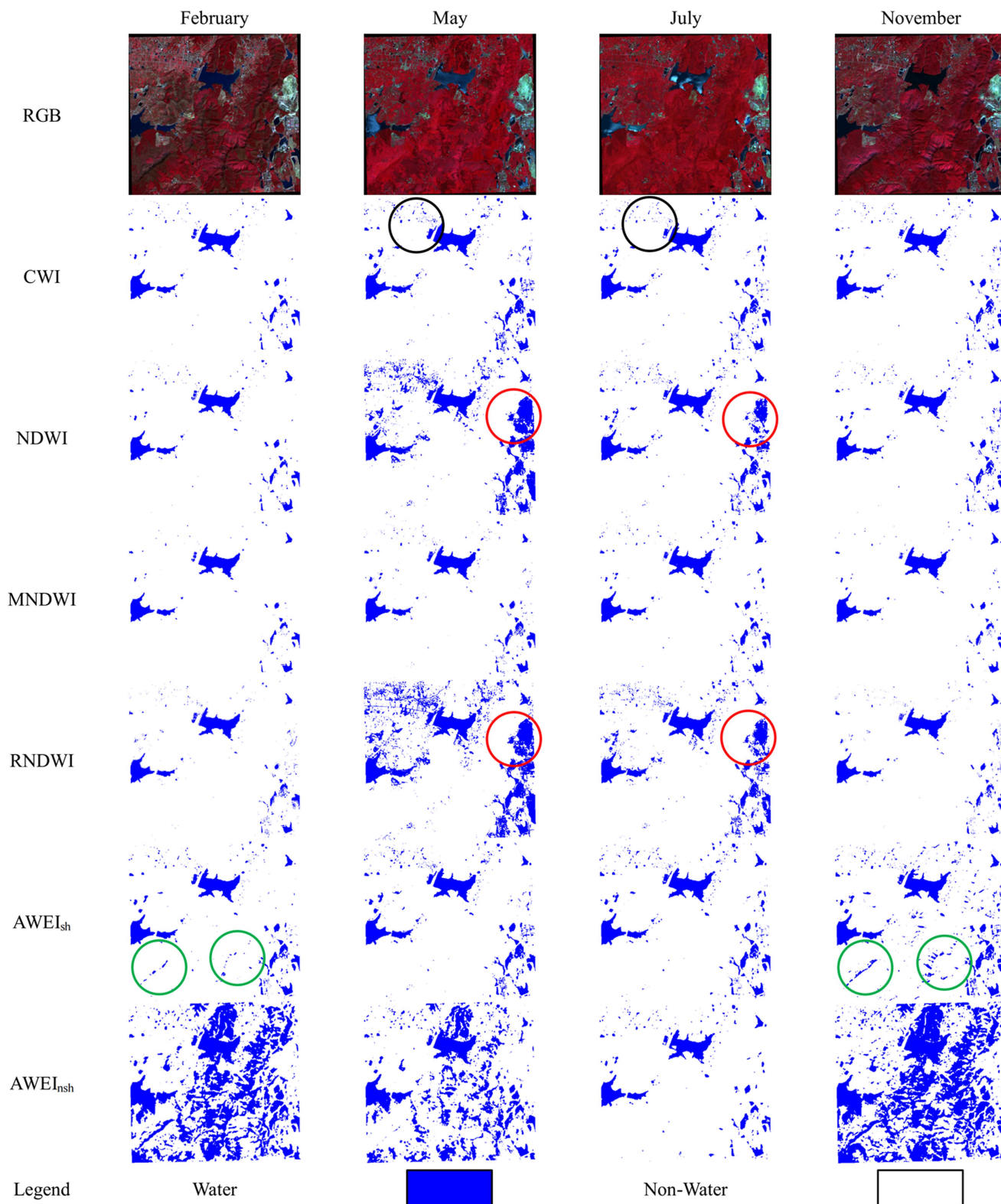


Fig. 8. Water extraction results in mountainous area.

TABLE IV
OA AND KAPPA IN VEGETATION AREA

Month		CWI	NDWI	MNDWI	RNDWI	AWEI _{sh}	AWEI _{insh}
February	OA(%)	97.13	95.69	92.82	84.21	91.39	95.69
	Kappa	0.94	0.91	0.85	0.68	0.83	0.91
May	OA(%)	96.26	88.24	89.30	78.07	94.65	96.26
	Kappa	0.92	0.74	0.78	0.50	0.89	0.92
July	OA(%)	96.88	92.41	95.98	91.07	95.54	96.43
	Kappa	0.94	0.84	0.92	0.82	0.91	0.93
November	OA(%)	96.69	96.08	94.58	91.87	93.07	94.28
	Kappa	0.93	0.92	0.89	0.83	0.86	0.89
Average	OA(%)	96.74	93.11	93.17	86.31	93.66	95.67
	Kappa	0.93	0.86	0.86	0.71	0.87	0.91

The highest value of all OA/Kappa.

TABLE V
OA AND KAPPA IN MOUNTAINOUS AREA

Month		CWI	NDWI	MNDWI	RNDWI	AWEI _{sh}	AWEI _{insh}
February	OA(%)	96.21	94.75	92.13	88.05	96.50	85.42
	Kappa	0.92	0.90	0.84	0.76	0.93	0.71
May	OA(%)	95.16	76.12	94.46	76.47	94.12	92.39
	Kappa	0.90	0.54	0.89	0.54	0.88	0.85
July	OA(%)	95.74	80.98	96.07	79.67	94.43	94.43
	Kappa	0.91	0.63	0.92	0.60	0.89	0.89
November	OA(%)	95.32	94.15	92.69	88.89	93.57	81.58
	Kappa	0.91	0.88	0.85	0.78	0.87	0.64
Average	OA(%)	95.61	86.50	93.84	83.27	94.66	88.46
	Kappa	0.91	0.74	0.88	0.67	0.89	0.77

The highest value of all OA/Kappa.

Owing to the unstable topography in the eastern segment of the experimental area, several water indices are affected to some extent. NDWI and RNDWI misclassified water, mountains, and shadows in the eastern section of the experimental region in May and July (as shown in red circles). In addition, AWEI_{sh} mistakenly classified mountain shadows as water in the southern part of the experimental area in both February and November (as shown in green circles). The AWEI_{insh} extraction results exhibit significant confusion and are unsuitable for water extraction in mountainous terrains. CWI and MNDWI demonstrate interference against terrain and shadows, with CWI exhibiting the ability to accurately identify small bodies of water in the northern region of the experimental area (as shown in black circles), outperforming MNDWI in terms of extraction performance.

Table V shows the water extraction accuracy in mountainous areas. The average OA of CWI was 95.61%, surpassing AWEI_{sh} by 0.95%. The average Kappa coefficient of CWI was 0.91, which was 0.0188 higher than that of AWEI_{sh}. In the four-month water extraction experiment, the OA and Kappa coefficients of MNDWI are 0.33% and 0.01 higher than CWI in July. In contrast, CWI consistently demonstrated the highest OA and Kappa coefficients among all the methods in the remaining seasons. Therefore, CWI was deemed more suitable for extracting dense time-sequences water in mountainous areas.

D. Application of CWI Frequency Method in Jiangsu Province

The CWI frequency method was employed for water extraction in Jiangsu Province after verifying the excellent performance of CWI in different environmental backgrounds and seasons. The average frequency distribution of the surface water in Jiangsu Province from 2019 to 2022 is shown in Fig. 9. It is

evident from Fig. 9 that the regions in Jiangsu Province characterized by high water frequency primarily encompass Lake Taihu, Lake Gaoyou, Lake Hongze, and the Yangtze River. These areas predominantly consist of permanent water. In addition, permanent water is also observed in the southern and northern regions of Jiangsu Province. Temporary and seasonal water are predominantly situated in central Jiangsu Province.

To conduct a more in-depth analysis of the frequency changes in water within Jiangsu Province, we have chosen Lake Taihu and a part of the Yangtze River as representative water. We have investigated the interannual fluctuation characteristics of these areas, as illustrated in Fig. 10. The average, permanent, and seasonal water areas of Lake Taihu and the Jiangsu section of the Yangtze River over the four years are shown in Fig. 11.

As depicted in Fig. 10(a) for the Lake Taihu area, the overall frequency of water exhibits an increasing trend from 2019 to 2022, indicating the progressive transition of seasonal water into permanent ones. In 2019 and 2020, specific areas within Lake Taihu (highlighted in the red box) depict low frequencies of water, attributed to the presence of hydrophobic organisms impacting water identification results. There are many livestock and poultry breeding areas in the eastern part of Taihu Lake. Livestock and poultry breeding will affect water quality and quantity, which directly led to the low frequency of water in this area during 2019 and 2020. As of 2022, the establishment of livestock and poultry breeding areas is basically prohibited. Water quality has gradually improved, and water frequency has increased significantly. In the relevant information display, it is observed that recent water environment improvement and protection measures in the Lake Taihu Basin have led to enhanced water quality and quantity. This aligns with the trends presented

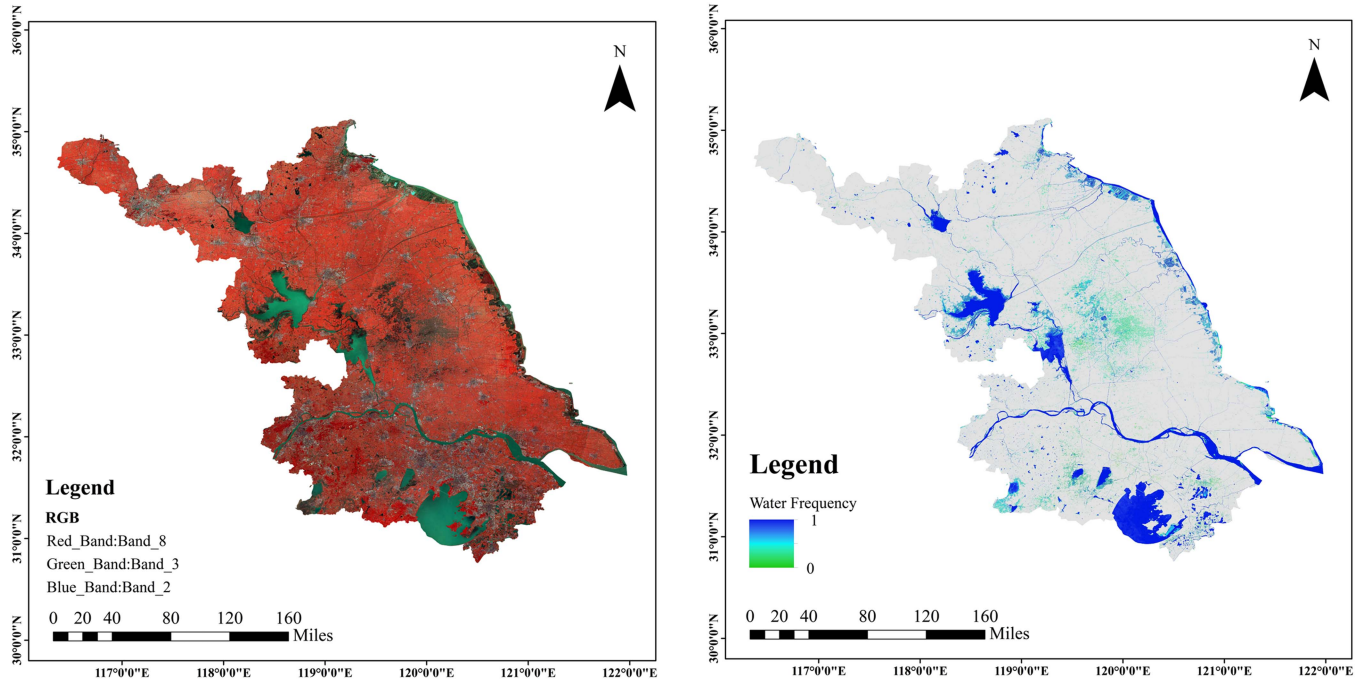


Fig. 9. RGB image and water frequency map of Jiangsu Province.

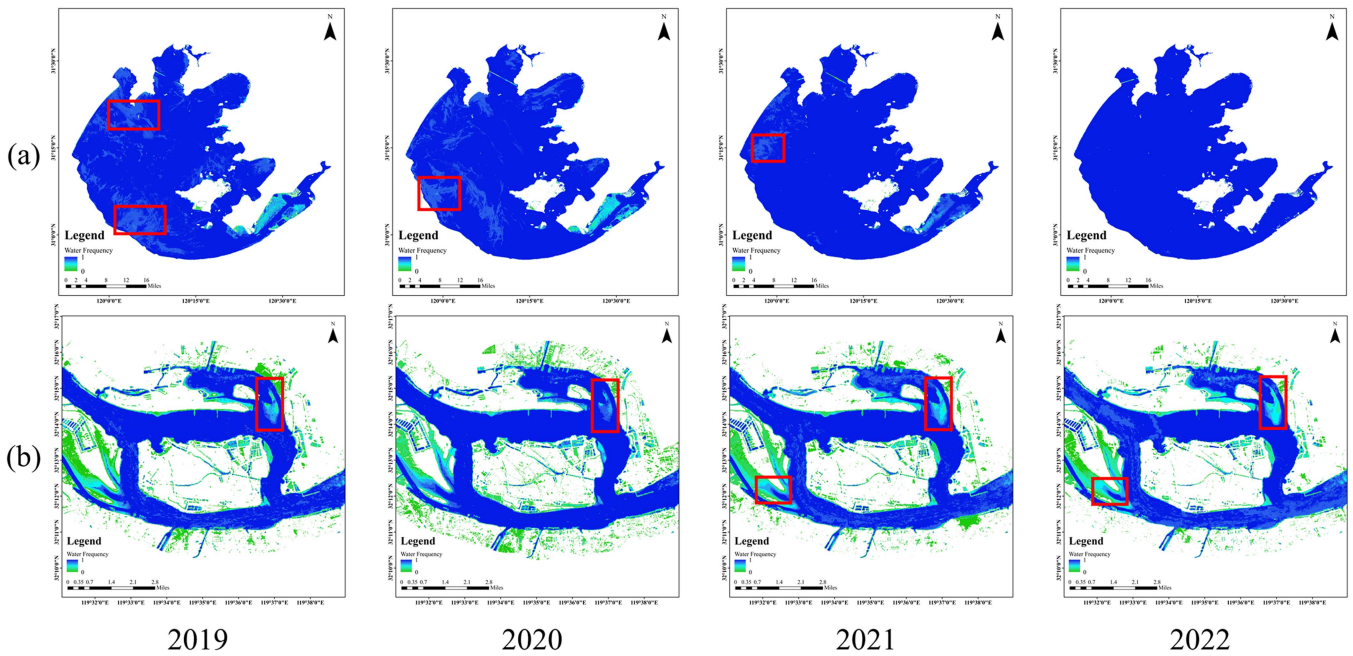


Fig. 10. Interannual frequency changes in the Lake Taihu region and a part of the Yangtze River from 2019 to 2022.

in Fig. 10. In the Yangtze River region [Fig. 10(b)], the primary channel of the Yangtze River is heavily silted, exhibiting intricate configurations. Within specific segments of the main channel, a reduction in water flow frequency is observed, coinciding with a gradual expansion of the sandbar area, as highlighted in the red box.

As depicted in Fig. 11(a), the seasonal water area in the Lake Taihu area is comparatively small and exhibits a declining

trend over the years. Concurrently, the permanent water area experiences a gradual increase, and the average water area demonstrates a fluctuating pattern characterized by an initial rise, decline, and subsequent increase. The relatively stable and steadily rising average water area suggests stable climate and ecological conditions in the Lake Taihu region, indicating effective water environment protection and well-managed water resources. Fig. 11(b) illustrates the water area in the Jiangsu

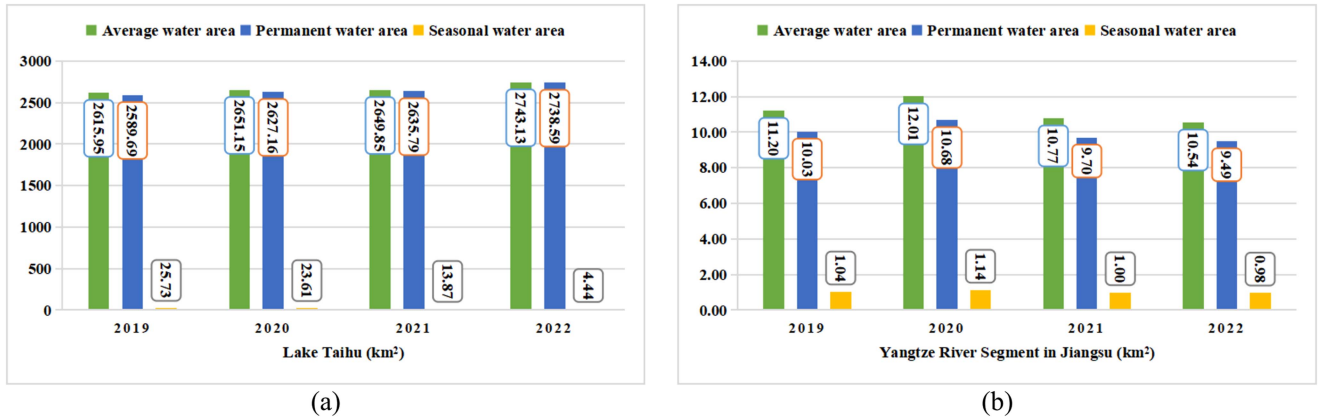


Fig. 11. Water area information.

section of the Yangtze River. The difference in seasonal water area in this section is minimal, with the permanent water area displaying an overall effectiveness trend. However, the average water area exhibits significant fluctuations, peaking at 12.01 km² in 2020 and decreasing to 10.54 km² in 2022. Attention should be directed towards refining the calculation management method for the Yangtze River Jiangsu section to ensure the continued health and sustainable use of water.

V. DISCUSSION

Through an investigation of various water indices, this study introduces the CWI, which is then integrated with the water frequency method for monitoring the dynamic changes in water. The extraction results and accuracy table substantiate the method's precision and efficiency. Nevertheless, it is imperative to engage in a more in-depth discussion on the performance of the CWI frequency model.

A. Performance Analysis of CWI

Each water index possesses distinct advantages. NDWI offers simplicity in operation [26], MNDWI enhances differentiation between water and buildings [27], RNDWI eliminates shadow influences [28], and AWEI augments the separability of water and nonwater pixels [29]. Leveraging these strengths allows CWI demonstrates proficient water extraction performance across diverse backgrounds. The resilience and universality of the model to noise, changes, or specific scenarios in the data may be confirmed by extracting water from data across time, seasons, and geographical locations and assessing the accuracy of the extraction findings.

In Tables III–V, it is evident that in urban area, CWI exhibits a maximum discrepancy in the OA of 1.76% and a maximum variance in the Kappa coefficient of 0.03. In the vegetation area, these values were 3.34% and 0.02, respectively, while in mountainous area, they were 0.87% and 0.02, respectively. The boxplot (Fig. 12) illustrates the total classification accuracy and Kappa coefficient of the various water extraction techniques. Observing the box plot distribution reveals that the CWI extraction results exhibit greater stability in terms of accuracy across various seasons and regions. This indicates that the CWI

consistently produces reliable water extraction results in diverse environments with a relatively high level of accuracy. The medians in the boxplots represent the central tendencies of the data distribution. The higher medians of both OA and Kappa for CWI signify that its average performance approached the ideal result more closely.

In conclusion, CWI exhibited superior spatiotemporal stability, resulting in more distinct water boundaries and reduced misextraction, as demonstrated through the statistical analysis of OA and Kappa coefficients. Thus, CWI is a reliable choice for water extraction across various seasons and geographic regions.

B. Applicability Analysis of CWI Frequency Method

To validate the effectiveness of the CWI in water extraction within a dense time-sequences, we opted for a comparison with the global surface water data product generated by Amy H. Pickens et al. [45] in 2020.

For comparison, representative regions within Jiangsu Province were selected as case studies to assess the water frequency results yielded by both methods for 2019 (Figs. 13–15). First, due to the lower spatial resolution of Landsat images compared to Sentinel-2 images, discernible noise is evident at the water boundary in Pickens' study. Fig. 13 illustrates that Pickens' method generally exhibits low water frequency and poor water continuity, indicating a limited water identification capability. In contrast, our method excels in identifying most of water. In Fig. 14, the water frequency results in the eastern coastal area of Jiangsu Province are presented. Pickens' results appear indistinct, failing to discern the coastline. In contrast, our method distinctly captures changes in water frequency along coastal areas and accurately delineates the coastline boundaries. Fig. 15(a) and (b) represent the silt accumulation area, and our method demonstrates an exceptional discrimination ability. Furthermore, Fig. 15(c) highlights the capacity of the proposed method to clearly depict the water frequency changes at the end of the Yangtze River tributaries, in contrast to the relatively blurred frequency changes observed using Pickens' method.

Pickens employed all Landsat image bands in conjunction with NDWI and MNDWI to classify remote sensing images, enabling the distinction of clouds, snow, fog, land, shadows,

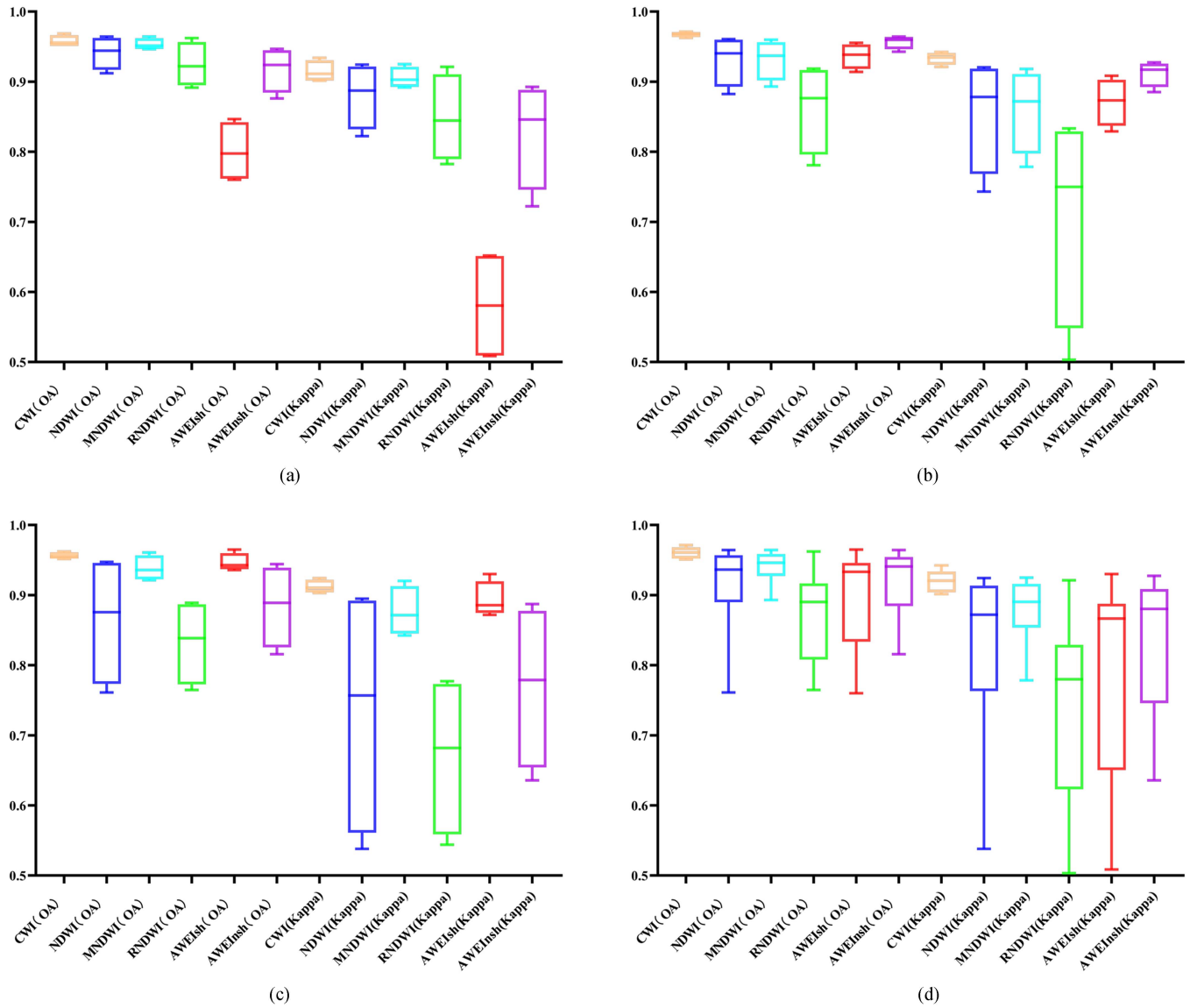


Fig. 12. OA and Kappa coefficient box plot. (a) Urban area. (b) Vegetation area. (c) Mountainous area. (d) Overall result.

and water. Hence, Pickens' method is restricted to utilizing Landsat data for water extraction, leading to unimproved spatial resolution in the extracted results. Conversely, our approach is adaptable to various satellite data types, providing flexibility in selection based on specific requirements. Moreover, it does not account for variations in vegetation, buildings, and water, leading to subpar water extraction results. However, Pickens added too much feature information to the classification model, causing noise to be mixed into the model, resulting in reduced accuracy.

C. Study Limitations

The CWI frequency method offers numerous advantages for water extraction and the analysis of dynamic changes in water. However, certain aspects require further improvement.

The CWI model was constructed by incorporating five indices capable of mitigating noise from sources such as buildings, vegetation, and mountain shadows. However, it may be necessary to select and adjust the water indices to meet specific requirements. For instance, this model cannot identify turbid water-containing substances, such as algae, suspended matter, and colloidal particles [46], [47], resulting in a lower water detection frequency in certain areas. Moreover, considering the plethora of available water indices, further optimization of the CWI model is warranted.

The evaluation of CWI performance in this experiment primarily concentrated on the extraction performance of water across diverse environmental backgrounds. However, there is a notable absence of further verification regarding its performance in extracting different types of water, such as lakes, slender rivers, and reservoirs. Therefore, future research should include

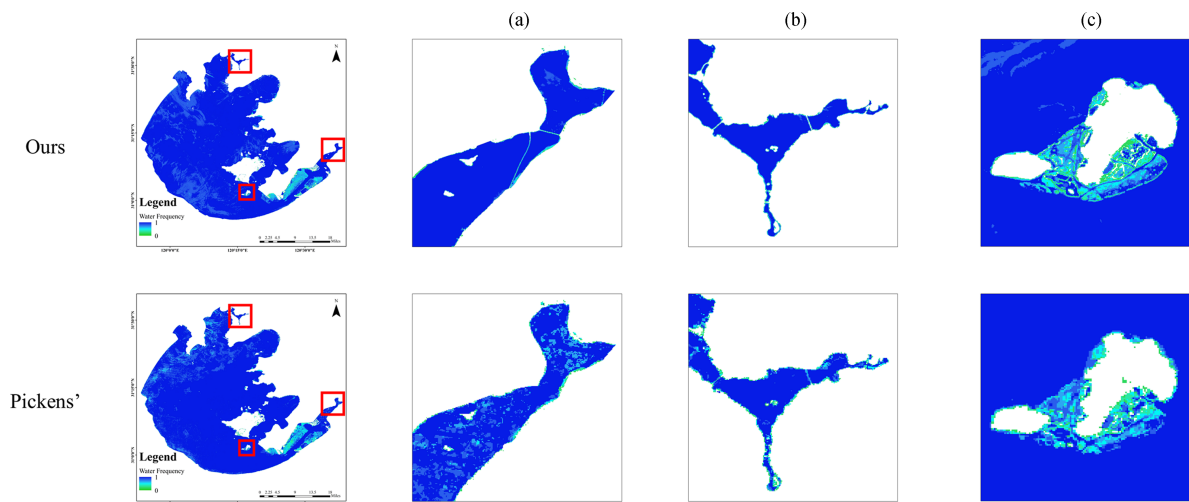


Fig. 13. Water frequency analysis in the Lake Taihu area. (a)–(c) Comparison of local details in the experimental area.

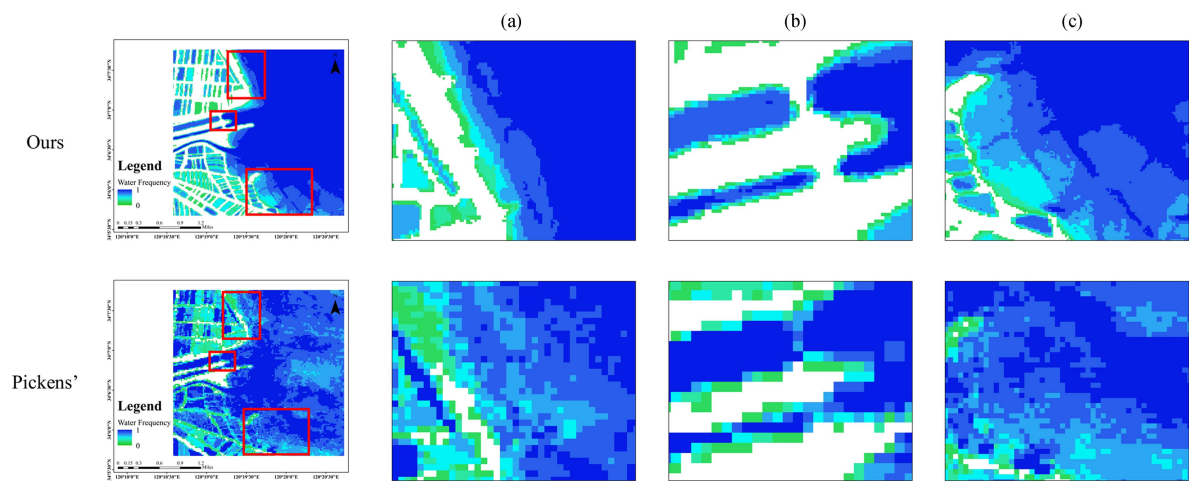


Fig. 14. Water frequency analysis in coastal area of Jiangsu Province. (a)–(c) Comparison of local details in the experimental area.

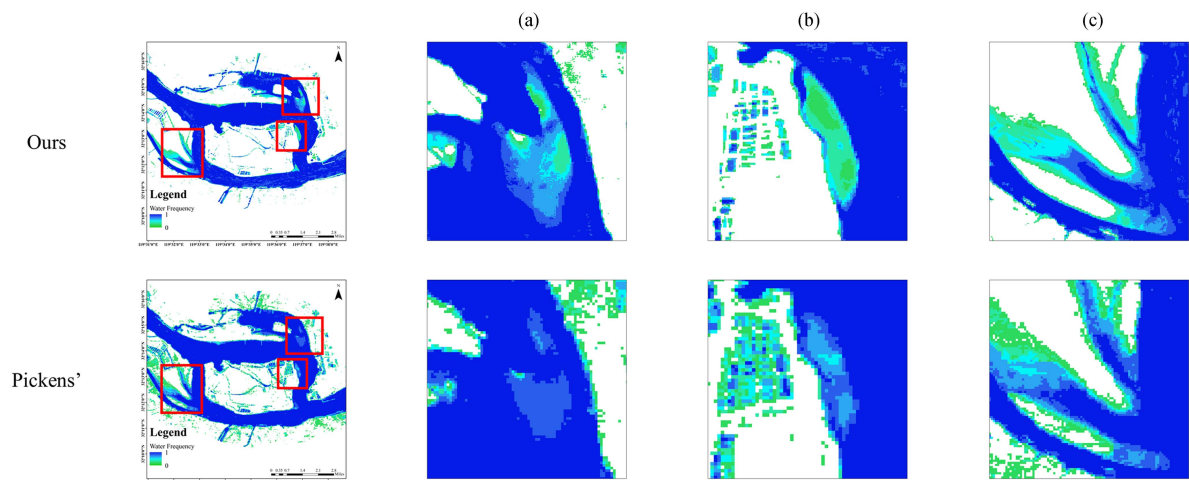


Fig. 15. Water frequency analysis in the Jiangsu section of the Yangtze River. (a)–(c) Comparison of local details in the experimental area.

experimental validation and model optimization across various water types.

The accuracy of remote sensing water extraction is directly influenced by the determination of the threshold. In this study, the Otsu algorithm is employed for threshold determination. However, it is noteworthy that the Otsu algorithm necessitates extensive calculations, potentially leading to the loss of target details and edge blurring. In instances where there is minimal contrast in spectral grayscale values between the water and background features in the study area, particularly when water pixels occupy a larger area, the accuracy of the Otsu algorithm may decrease. Furthermore, variations in water quality, experimental areas, and remote sensing images can also impact the threshold. Therefore, future research should focus on optimizing the threshold determination method to enhance the accuracy of water extraction.

VI. CONCLUSION

This study evaluated the applicability of various water indices and introduced a CWI model. In addition, the extraction performance of the CWI across diverse water backgrounds was investigated. Furthermore, this research introduced a CWI frequency method to assess dynamic water changes using the CWI model.

The application of the CWI frequency method, implemented on the GEE platform, yielded outstanding results in large-scale water extraction. Notably, the utilization of CWI produces more precise water boundaries, effectively mitigating the impact of intricate backgrounds. Experimental results revealed that, on average, the classification accuracy in urban, vegetation, and mountainous area was 95.77%, 96.74%, and 95.61%, respectively, while the average Kappa coefficient reached 0.91, 0.93, and 0.91, respectively. The water extraction accuracy outperformed that of the other indices. The stability of water extraction across diverse backgrounds and seasons underscores CWI's exceptional stability of CWI compared with alternative water indices. Consequently, the CWI is capable of achieving heightened precision in water monitoring across varying seasons and complex backgrounds. In the future, CWI frequency method can be applied for large-scale, high-precision, and long-term water dynamic monitoring.

REFERENCES

- [1] J. F. Pekel, A. Cottam, N. Gorelick, and A. S. Belward, "High-resolution mapping of global surface water and its long-term changes," *Nature*, vol. 540, no. 7633, pp. 418–422, Dec. 2016.
- [2] Y. Yang et al., "Landsat 8 OLI image based terrestrial water extraction from heterogeneous backgrounds using a reflectance homogenization approach," *Remote Sens. Environ.*, vol. 171, pp. 14–32, 2015.
- [3] Z. Zhang et al., "Automated surface water extraction combining Sentinel-2 imagery and OpenStreetMap using presence and background learning (PBL) algorithm," *IEEE J. Sel. Topics Appl. Earth Observ. Remote Sens.*, vol. 12, no. 10, pp. 3784–3798, Oct. 2019.
- [4] N. Xu, "Detecting coastline change with all available Landsat data over 1986–2015: A case study for the state of Texas, USA," *Atmosphere*, vol. 9, no. 3, pp. 107–126, 2018.
- [5] Y. Chen, R. Fan, X. Yang, J. Wang, and A. Latif, "Extraction of urban water bodies from high-resolution remote-sensing imagery using deep learning," *Water*, vol. 10, no. 5, pp. 585–604, 2018.
- [6] X. Yang, Q. Qin, P. Grussenmeyer, and M. Koehl, "Urban surface water body detection with suppressed built-up noise based on water indices from Sentinel-2 MSI imagery," *Remote Sens. Environ.*, vol. 219, pp. 259–270, 2018.
- [7] C. A. Rishikeshan and H. Ramesh, "An automated mathematical morphology driven algorithm for water body extraction from remotely sensed images," *ISPRS J. Photogrammetry Remote Sens.*, vol. 146, pp. 11–21, 2018.
- [8] Y. Li, B. Dang, Y. Zhang, and Z. Du, "Water body classification from high-resolution optical remote sensing imagery: Achievements and perspectives," *ISPRS J. Photogrammetry Remote Sens.*, vol. 187, pp. 306–327, 2022.
- [9] N. Xu and P. Gong, "Significant coastline changes in China during 1991–2015 tracked by Landsat data," *Sci. Bull.*, vol. 63, no. 14, pp. 883–886, Jul. 2018.
- [10] K. Jia, W. Jiang, J. Li, and Z. Tang, "Spectral matching based on discrete particle swarm optimization: A new method for terrestrial water body extraction using multi-temporal Landsat 8 images," *Remote Sens. Environ.*, vol. 209, pp. 1–18, 2018.
- [11] E. Goumehei and W. Yan, "Applying DEM data to improve performance of water extraction indices using Landsat 8 OLI images in mountainous area," in *Proc. Int. Electron. Symp.*, 2016, pp. 455–458.
- [12] J. Lan, L. Zhang, and Y. Guo, "Spectral index-spatially correlated water extraction method based on GF-5 hyperspectral satellite images," in *Proc. 3rd Int. Conf. Geol., Mapping, Remote Sens.*, 2022, pp. 613–618.
- [13] S. An and X. Rui, "A high-precision water body extraction method based on improved lightweight U-Net," *Remote Sens.*, vol. 14, no. 17, 2022, Art. no. 4127.
- [14] T. D. Acharya, D. H. Lee, I. T. Yang, and J. K. Lee, "Identification of water bodies in a Landsat 8 OLI image using a J48 decision tree," *Sensors*, vol. 16, no. 7, Jul. 2016, Art. no. 1075.
- [15] Q. Liu, C. Huang, Z. Shi, and S. Zhang, "Probabilistic river water mapping from Landsat-8 using the support vector machine method," *Remote Sens.*, vol. 12, no. 9, 2020, Art. no. 1374.
- [16] B. Li et al., "An object-oriented method for extracting single-object aquaculture ponds from 10 m resolution Sentinel-2 images on Google Earth Engine," *Remote Sens.*, vol. 15, no. 3, pp. 856–879, 2023.
- [17] X. Sui, Z. Li, G. Tang, Z.-L. Yang, and D. Niyogi, "Disentangling error structures of precipitation datasets using decision trees," *Remote Sens. Environ.*, vol. 280, 2022, Art. no. 113185.
- [18] C. Cortes and V. Vapnik, "Support-vector networks," *Mach. Learn.*, vol. 20, pp. 273–297, 1995.
- [19] D. A. Maciel, C. C. F. Barbosa, E. M. L. M. Novo, R. F. Júnior, and F. N. Begliomini, "Water clarity in Brazilian water assessed using Sentinel-2 and machine learning methods," *ISPRS J. Photogrammetry Remote Sens.*, vol. 182, pp. 134–152, 2021.
- [20] H. Guo, S. Tian, J. J. Huang, X. Zhu, B. Wang, and Z. Zhang, "Performance of deep learning in mapping water quality of Lake Simcoe with long-term Landsat archive," *ISPRS J. Photogrammetry Remote Sens.*, vol. 183, pp. 451–469, 2022.
- [21] J. Fei, J. Liu, L. Ke, W. Wang, P. Wu, and Y. Zhou, "A deep learning-based method for mapping alpine intermittent rivers and ephemeral streams of the Tibetan Plateau from Sentinel-1 time series and DEMs," *Remote Sens. Environ.*, vol. 282, 2022, Art. no. 113271.
- [22] Y. Wang, Z. Li, C. Zeng, G.-S. Xia, and H. Shen, "An urban water extraction method combining deep learning and Google Earth Engine," *IEEE J. Sel. Topics Appl. Earth Observ. Remote Sens.*, vol. 13, pp. 769–782, 2020.
- [23] F. Isikdogan, A. C. Bovik, and P. Passalacqua, "Surface water mapping by deep learning," *IEEE J. Sel. Topics Appl. Earth Observ. Remote Sens.*, vol. 10, no. 11, pp. 4909–4918, Nov. 2017.
- [24] W. Li et al., "A comparison of land surface water mapping using the normalized difference water index from TM, ETM+ and ALI," *Remote Sens.*, vol. 5, no. 11, pp. 5530–5549, 2013.
- [25] Y. Meng, P. Du, X. Wang, X. Bai, and S. Guo, "Monitoring human-induced surface water disturbance around Taihu Lake since 1984 by time series Landsat images," *IEEE J. Sel. Topics Appl. Earth Observ. Remote Sens.*, vol. 13, pp. 3780–3789, 2020.
- [26] S. K. McFeeters, "The use of the normalized difference water index (NDWI) in the delineation of open water features," *Int. J. Remote Sens.*, vol. 17, no. 7, pp. 1425–1432, 2007.
- [27] H. Xu, "Modification of normalised difference water index (NDWI) to enhance open water features in remotely sensed imagery," *Int. J. Remote Sens.*, vol. 27, no. 14, pp. 3025–3033, 2007.
- [28] C. Ronglong, L. Cunjun, and L. Liangyun, "Extracting miyun reservoir's water area and monitoring its change based on a revised normalized different water index," *Sci. Surveying Mapping*, vol. 33, no. 2, pp. 158–160, 2008.

- [29] G. L. Feyisa, H. Meilby, R. Fensholt, and S. R. Proud, "Automated water extraction index: A new technique for surface water mapping using Landsat imagery," *Remote Sens. Environ.*, vol. 140, pp. 23–35, 2014.
- [30] L. Li, H. Su, Q. Du, and T. Wu, "A novel surface water index using local background information for long term and large-scale Landsat images," *ISPRS J. Photogrammetry Remote Sens.*, vol. 172, pp. 59–78, 2021.
- [31] S. Feng et al., "Long-term dense Landsat observations reveal detailed waterbody dynamics and temporal changes of the size-abundance relationship," *J. Hydrol.: Regional Stud.*, vol. 41, 2022, Art. no. 101111.
- [32] P. Rao, W. Jiang, Y. Hou, Z. Chen, and K. Jia, "Dynamic change analysis of surface water in the Yangtze River Basin based on MODIS products," *Remote Sens.*, vol. 10, no. 7, 2018, Art. no. 1025.
- [33] Z. Wang, M. Jia, N. Chen, and W. Wang, "Long-term surface water dynamics analysis based on Landsat imagery and the Google Earth Engine platform: A case study in the middle Yangtze River Basin," *Remote Sens.*, vol. 10, no. 10, 2018, Art. no. 1635.
- [34] V. Soti, A. Tran, J.-S. Bailly, C. Puech, D. L. Seen, and A. Bégué, "Assessing optical earth observation systems for mapping and monitoring temporary ponds in arid areas," *Int. J. Appl. Earth Observ. Geoinform.*, vol. 11, no. 5, pp. 344–351, 2009.
- [35] Z. Wang, J. Liu, J. Li, Y. Meng, Y. Pokhrel, and H. Zhang, "Basin-scale high-resolution extraction of drainage networks using 10-m Sentinel-2 imagery," *Remote Sens. Environ.*, vol. 255, 2021, Art. no. 112281.
- [36] M. Main-Knorn et al., "Sen2Cor for Sentinel-2," *Proc. SPIE*, vol. XXIII, 2017, Art. no. 1042704.
- [37] A. Huete, K. Didan, T. Miura, E. P. Rodriguez, X. Gao, and L. G. Ferreira, "Overview of the radiometric and biophysical performance of the MODIS vegetation indices," *Remote Sens. Environ.*, vol. 83, no. 1/2, pp. 195–213, 2002.
- [38] N. Otsu, "A threshold selection method from gray-level histograms," *IEEE Trans. Syst.*, vol. 9, no. 1, pp. 62–66, Jan. 1979.
- [39] W. Tang et al., "Improved spectral water index combined with Otsu algorithm to extract muddy coastline data," *Water*, vol. 14, no. 6, pp. 855–869, 2022.
- [40] C. Wang, W. Jiang, Y. Deng, Z. Ling, and Y. Deng, "Long time series water extent analysis for SDG 6.6.1 based on the GEE platform: A case study of Dongting Lake," *IEEE J. Sel. Topics Appl. Earth Observ. Remote Sens.*, vol. 15, pp. 490–503, 2022.
- [41] Y. Deng, W. Jiang, Z. Tang, Z. Ling, and Z. Wu, "Long-term changes of open-surface water bodies in the Yangtze River Basin based on the Google Earth Engine cloud platform," *Remote Sens.*, vol. 11, no. 19, 2019, Art. no. 2213.
- [42] Y. Zhou et al., "Continuous monitoring of lake dynamics on the Mongolian Plateau using all available Landsat imagery and Google Earth Engine," *Sci. Total Environ.*, vol. 689, pp. 366–380, Nov. 2019.
- [43] X. Yang et al., "Monthly estimation of the surface water extent in France at a 10-m resolution using Sentinel-2 data," *Remote Sens. Environ.*, vol. 244, 2020, Art. no. 111803.
- [44] X. Yang, S. Zhao, X. Qin, N. Zhao, and L. Liang, "Mapping of urban surface water bodies from Sentinel-2 MSI imagery at 10 m resolution via NDWI-based image sharpening," *Remote Sens.*, vol. 9, no. 6, pp. 596–614, 2017.
- [45] A. H. Pickens et al., "Mapping and sampling to characterize global inland water dynamics from 1999 to 2018 with full Landsat time-series," *Remote Sens. Environ.*, vol. 243, 2020, Art. no. 111792.
- [46] D. D. Ngoc et al., "Coastal and inland water pixels extraction algorithm (WiPE) from spectral shape analysis and HSV transformation applied to Landsat 8 OLI and Sentinel-2 MSI," *Remote Sens. Environ.*, vol. 223, pp. 208–228, 2019.
- [47] Z. Li, X. Zhang, and P. Xiao, "Spectral index-driven FCN model training for water extraction from multispectral imagery," *ISPRS J. Photogrammetry Remote Sens.*, vol. 192, pp. 344–360, 2022.



Hanyuan Liu received the B.S. degree in surveying and mapping engineering in 2022 from Hohai University, Nanjing, China, where he is currently working toward the master's degree in surveying and mapping science and technology with the School of Earth Sciences and Engineering.

His main research interests are spatial-temporal variation analysis of remote sensing of water resources and remote sensing of the ecological environment.

Yue Shi received the Ph.D. degree in municipal engineering from the Army Engineering University of PLA, Nanjing, China, in 2017.

She is currently an Associate Professor with the Army Engineering University of PLA. Her main research interests include remote-sensing of water quality and water supply treatment.

Qinnan Chang received the M.S. degree in civil and hydraulic engineering from Hohai University, Nanjing, China, in 2022.

She is currently working with Jincheng Urban District Housing and Urban-Rural Development Bureau, Beijing, China.

Rufat Guluzade received the M.S. degree in geodesy and cartography engineering from Baku State University, Baku, Azerbaijan, in 2018. He is currently working toward the Ph.D. degree in geodesy and survey engineering with the School of Earth Sciences and Engineering, Hohai University, Nanjing, China.

His main research interests include remote sensing products of climate, geospatial analysis on climate data, and land use land cover mapping.

Xin Pan received the Ph.D. degree in cartography and geographical information system from the Nanjing Institute of Geography and Limnology, Chinese Academy of Sciences, Nanjing, China, in 2016.

He is currently an Associate Professor with the College of Geography and Remote Sensing, Hohai University, Nanjing, China. His research interests include remote-sensing retrieval and validation of land surface evapotranspiration and net radiation.

Nan Xu received the Ph.D. degree in coastal remote sensing from the Department of Earth System Science, Tsinghua University, Beijing, China, in 2019.

In 2017, he was a Visiting Scholar with UNSW Canberra. He is currently an Associate Professor with the College of Geography and Remote Sensing, Hohai University, Nanjing, China. He mainly focuses on surface water remote sensing.

Penghua Hu received the B.S. degree in surveying and mapping engineering in 2021 from Hohai University, Nanjing, China, where he is currently working toward the master's degree in surveying and mapping science and technology with the School of Earth Sciences and Engineering.

His main research interest is thermal infrared remote sensing data fusion.

Xuechun Kong received the B.S. degree in remote sensing science and technology from Shandong Agricultural University, Taian, China, in 2021. She is currently working toward the master's degree in surveying and mapping science and technology with the School of Earth Sciences and Engineering, Hohai University, Nanjing, China.

Her main research interest is soil moisture downscaling.

Yingbao Yang received the Ph.D. degree in cartography and geographical information system from the Nanjing Institute of Geography and Limnology, Chinese Academy of Sciences, Nanjing, China, in 2005.

In 2013, she was a Visiting Scholar with Michigan State University, East Lansing, MI, USA. She is currently a Professor with the College of Geography and Remote Sensing, Hohai University, Nanjing, China. Her main research interests include thermal infrared remote sensing, processing of remote sensing image data, remote sensing of surface water, and thermal environment.